This work was partially supported by the Defense Nuclear Agency.

Edited by Glenda Ponder, ESS Division

LA-9688-MS

UC-35
Issued: February 1983

Concentric Nuclear Explosions

Eric M. Jones
Rodney W. Whitaker
John W. Kodis

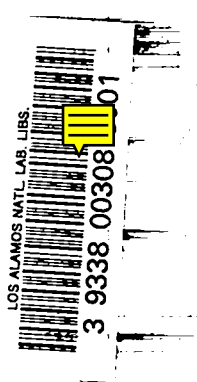

Los Alamos National Laboratory
Los Alamos, New Mexico 87545

CONCENTRIC NUCLEAR EXPLOSIONS

by

Eric M. Jones, Rodney W. Whitaker, and John W. Kodis

ABSTRACT

We have done numerical calculations of two co-located nuclear bursts separated by 5 s in time. The yields were both 1.2 Mt. At the time of the second burst, the central density in the fireball has dropped to 1/27th of atmospheric density. The distance to which energy is deposited increases as the cube root of the density so the initial radius of the hydrodynamic shock of the second burst is about three times that of the first burst. Similarly, the reduced density has a profound effect on the radiative history of the second burst. In fact, the second burst has a power-time history comparable to a single burst at similar density in the unperturbed atmosphere -- one at 30-40 km. The second burst radiates 60% of its energy compared with roughly 28% for the first burst.

I. INTRODUCTION

We have done a numerical simulation of two co-located 1.2-Mt nuclear explosions separated by 5 s in time. The calculations were done with the one-dimensional (spherical symmetry), coupled radiation-transport/hydrodynamics program RADFLO (Zinn 1973). We use tables of equation of state and opacity data for dry air. The program has successfully reproduced atmospheric nuclear test data and, with careful attention to numerical resolution, agrees well with the predictions of appropriate analytic results (e.g., jump conditions, blast-wave scaling).

II. FIRST BURST

Single-burst evolution has been described by Glasstone (1964), Brode (1968), Zinn (1973) and others. For the present set of calculations we have chosen to model a 1000-kg, 1.2-Mt source. The choice is rather arbitrary.

Initially, half the energy resides in thermal energy of the device and half as kinetic energy of the expanding (850 km/s) weapon debris. Initial energy deposition in the ambient air is due to x rays radiated by the hot source. At the end of x-ray deposition the 0.3 eV temperature contour is at 100-m radius although the steepest gradients of temperature and pressure are near 30 m.

The hot core grows by radiative expanson for the first 100 μs. At that time the core radius is 56 m and its characteristic temperature is 60 eV. At the same time the expanding weapon debris has reached 19-m radius. The sound speed in the core is 59.4 km/s compared with particle speeds of 43 km/s in the debris shock; the debris shock is rather weak with a Mach number (shock speed/ sound speed) of only 1.5. Profiles of velocity, pressure, density, and temperature at 100 μs are shown in in Fig. 1. Note that a hydrodynamic shock has begun to form at the core edge.

The hydrodynamic shock forms when the radiative expansion speed drops below ambient sound speed. Prior to this time radiative expansion is sufficiently rapid that no hydrodynamic signal can keep ahead of the radiative front. At 100 μs the core expansion speed is of the order of 0.5 km/s while the sound speed just outside the core is 3.5 km/s.

Formation of the shock marks transition to the hydrodynamic phase of expansion. Characteristics of the expansion are summarized in Fig. 2. The figure includes shock radius (R_s), density (ρ_s), particle velocity (U_s), and pressure (P_s); central pressure (P_c) and density (ρ_c); total thermal power (P_{TH}) and the integrated radiative loss ($\int P_{TH} dt$).

The radiative output remains unaltered by the hydrodynamic shock until the shock becomes optically thick at about 0.7 ms. Subsequent brightness variations are determined by the interplay of shock strength (Zinn and Anderson 1973), fireball area, and the optical thickness of the fireball (Zinn 1973). Although the derived power-time curve during the first maximum is dominated by fluctuations of numerical origin (high-resolution calculations show very small fluctuations), the fireball reaches first maximum near 3.5 ms. By this time the fireball has grown to 133 m and is well into the classical blast-wave phase (Taylor 1950, Brode 1955, Sedov 1959). Examination of the shock radius history in Fig. 2 shows that the fireball entered the blast-wave phase ($R \alpha t^{0.4}$) at 2 ms

when the radius was 110 m, twice the core radius when the hydrodynamic shock formed.*

Profiles of the state variables (density, pressure, temperature) and of velocity are given in Fig. 3 for 40 ms, a time in the midst of the blast-wave phase. Although the calculation has only modest resolution in the shock front (δr = 60 cm), jump conditions are near those expected from the shock velocity (v_s = 3.34 km/s = 0.4 R_s/t), the ambient sound speed (350 m/s) and the ratio of specific heats in the shocked gas (γ_s = 1.261). For example, the peak pressure is low by only 2%.

Eventually, as the shock wave weakens and the fireball becomes transparent (near the time of second maximum = 1 s), fireball evolution is no longer well-described by the blast-wave similarity solution. When the shock weakens to the point that entrained air is no longer heated above 0.3 eV, the shock ceases to be luminous and detaches ("shock breakaway") from the visible fireball surface. This happens at about 40 ms in the present calculation. Further, as the central pressure drops, positive pressure gradients ($\frac{dP}{dr} > 0$) create inward acceleration, slowing the growth of the visible fireball. The 0.3 eV contour begins to move inward (albeit at only a few meters per second) at about 1.5 s, near the time that the central pressure drops below atmospheric pressure. The central pressure falls to about 75% of ambient at 3 s and then recovers as the fireball shrinks. Profiles at 5 s, just before the second burst, are presented in Fig. 4.

III. SECOND BURST

Five seconds after the first explosion, an identical source was placed at the center of the computing mesh. Because expansion of the first fireball had

*This fireball initially grew by radiative expansion and entered the blast-wave phase when roughly 8 times the mass of the fireball core had been swept up by the shock. Wilke (1982) discusses the evolution of microfireballs (10^{-12} kt) generated by the laser-induced explosions of micron-sized glass spheres. These fireballs, which have no radiative expansion phase, also begin the blast-wave phase when the shock has swept up air about 8 times the mass of the glass spheres.

created large cells in the interior, we rezoned the inner mesh to give cell widths of roughly 5 m.

The first burst created an x-ray heated core of roughly 30-m radius, which then doubled in size by radiative expansion. By the time the hydrodynamic shock formed at 0.1 ms, the core radius was 55 m. We would expect that distances reached during the radiative phase would scale inversely with the cube root of the density. With the central density reduced a factor of 27 from atmospheric density, we would expect an initial core radius of 90 m and a radius for hydrodynamic shock formation of 165 m. The temperature profiles for both bursts at the end of x-ray depositon and at shock formation are shown in Fig. 5. The results are close to those expected from simple density scaling.

Evolution of the second burst begins with the x-ray deposition described above and with rapid expansion of the weapon debris. Figure 6, which gives radial contours of density as a function of time, clearly shows the debris shock at roughly 45 m at 0.1 ms after the second burst. The hydrodynamic shock begins to form at 200 m at about 0.5 ms. The debris shock dissipates on a time scale of milliseconds due to both the general expansion induced by the hydrodynamic shock and the infall produced by the rapid depressurization of the center during initial debris expansion.

The density profile inside the pre-existing fireball is fairly flat. The edge of the density well is several hundred meters from the burst point. In such a relatively homogeneous region we would expect the second burst to begin blast-wave expansion at 400 m -- about twice the core radius. Sedov (1959:p.260 ff) and others have shown that spherical shock waves moving into regions of variable density ($\rho \alpha R^{-w}$) have a shock front radius proportional to $t^{2.5-w}$. In Fig. 6 the shock wave expands as $t^{2/5}$ until it encounters the edge of the well, after which it expands more slowly. This is entirely consistent with the preceeding analysis ($w < 0$).

The general evolution of the second burst is summarized in Fig. 7. Perhaps the most outstanding difference between the two bursts is the far greater fraction of explosion energy radiated away by the second burst. Whereas the first burst radiated 330 kt (27.5%) of the 1200-kt explosion energy, the second radiated 720 kt (60%). The two power-time signatures are quite different.

The classic power-time curve of a low-altitude nuclear burst displays two peaks and is a phenomena of a strong luminous shock in air. As the ambient density is reduced, a strong shock develops farther and farther away from the burst point, i.e., it takes longer to sweep up a few core masses of air. Ultimately, for extremely low-density air, no hydrodynamic shock would form; the energy of the burst would go into prompt radiation and thermal energy. In such conditions the power-time curve would show one maximum, near t_o, and decrease after that time. As the burst height increases then, the power-time curve changes from the classic double-peak character to single-peak character. This is illustrated in Fig. 8, which shows the calculated power-time curve of a medium yield nuclear explosion at 50 km. The second burst in this study is in a density environment, which is characteristic of high altitude. The density in the well of the first burst at 5 s is similar to atmospheric density at 30 to 40 km. The power-time curve for the second burst at 5 s should have the character of a burst in this altitude region. Figure 9 is a calculated power-time curve for a medium yield nuclear burst at 35-km altitude. The similarity to the P_{TH} curve of Fig. 7 is striking. Thus, with less energy going into hydrodynamic motions, more is available to be radiated as thermal power. (Note the power values in Figs. 8 and 9.)

Finally, we address the late state of the double burst. How different is it from the final state of the first burst? The answer is -- not very different. Figure 10 shows the central temperature history for the double burst. The solid curve tracks the first burst. At 5 s the second burst produces a sharp spike and subsequent decay. We replot the decay with a 5-s time shift as the dashed curve.

Although there are early differences between the curves, these become minor after the fireballs become transparent (> 1 s). The reasons, of course, are that both fireballs are rapidly approaching pressure equilibrium with the atmosphere together with the fact that air is a poor radiator at these low, late-time temperatures. Similarly the central density returns to a value near 4×10^{-5} g/cm^3 5 s after each burst. Figure 11 shows profiles of the variables 5 s after the second burst. These should be compared with Fig. 4. Although the calculation obviously suffers from poor resolution, particularly in the two

shock waves, the overall structure (central values, width of the density well, location of shock peaks) are expected to be well determined.

IV. SUMMARY

A second, concentric nuclear explosion inside the density well of a prior explosion behaves normally provided that appropriate density scaling is observed and that the initial expansion occurs far from the walls. The power-time history is greatly modified by the perturbed environment. The minimum is virtually missing, first maximum is delayed, and power levels at second maximum are elevated. The total thermal output more than doubles.

REFERENCES

Brode, H. L., 1955, "Numerical Solutions of Spherical Blast Waves," J. Appl. Phys., V. 26, p. 766.

Brode, H. L., 1968, "Review of Nuclear Weapons Effects," Ann. Rev. Nuclear Science, V. 18, p. 153.

Glasstone, S., (ed.), 1964, The Effects of Nuclear Weapons (Rev. Ed), (Washington: U.S. Atomic Energy Commission).

Sedov, L. I., 1969, Similarity and Dimensional Methods in Mechanics, (New York, Academic Press).

Taylor, G. I., 1950, "The Formation of a Blast Wave by a Very Intense Explosion," Proc. Royal Soc., V. A201, p. 159.

Wilke, M. D., 1982, "Laser Shock Wave Generation, Propagation, and Interactions in Low Pressure Air," Los Alamos National Laboratory report LA-9182-T.

Zinn, J., 1973, "A Finite Difference Scheme for Time-Dependent Spherical Radiation Hydrodynamics Problems," J. Comp. Phys., V. 13, p. 569.

Zinn, J. and Anderson, R. C., 1973, "Structure and Luminosity of Strong Shock Waves in Air," Phys. Fluids, V. 16, p. 1639.

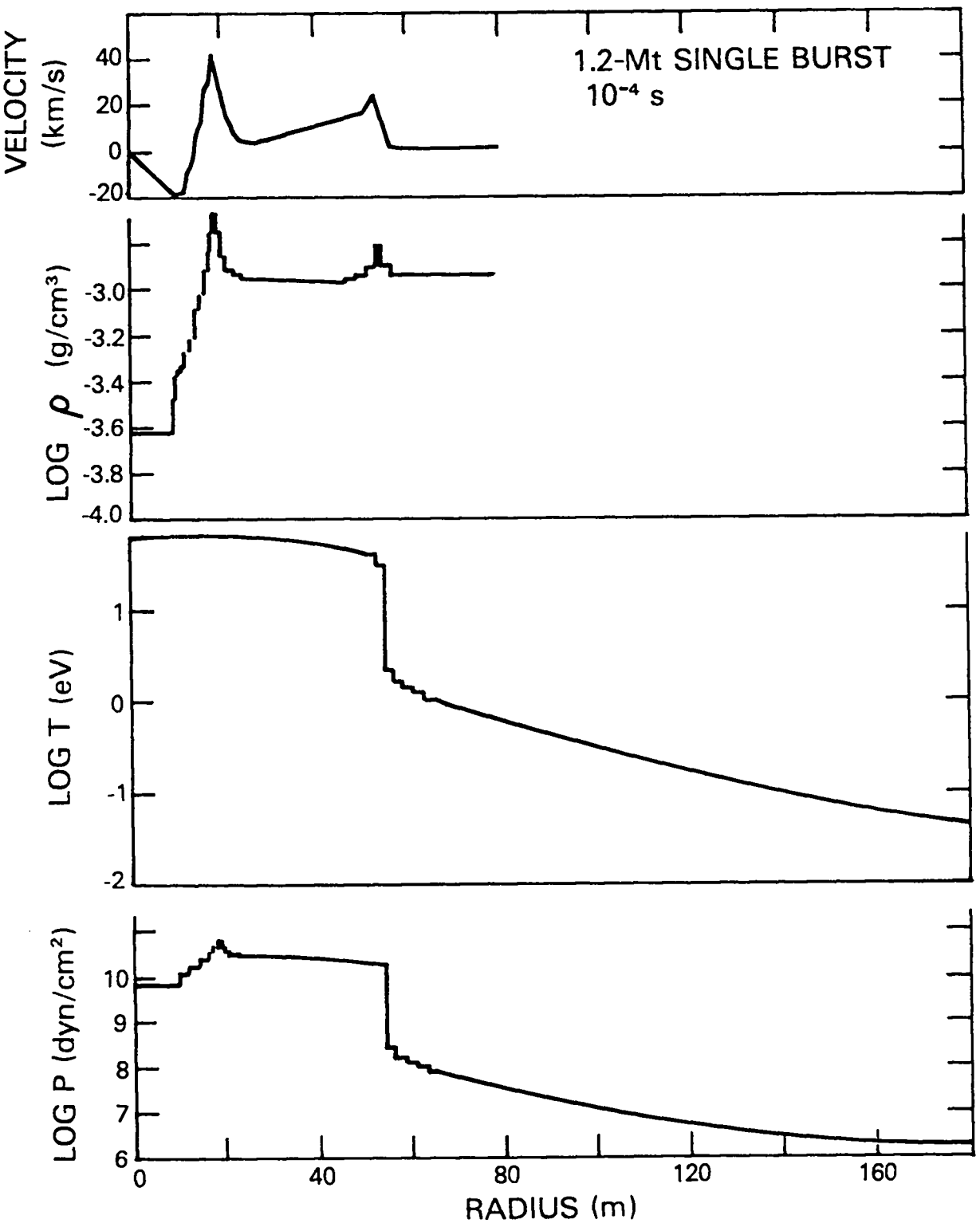

Fig. 1. Flow-field profiles at 0.1 ms for the first 1.2-Mt burst computed with RADFLO. The hydrodynamic shockwave has just begun to form near 56-m radius.

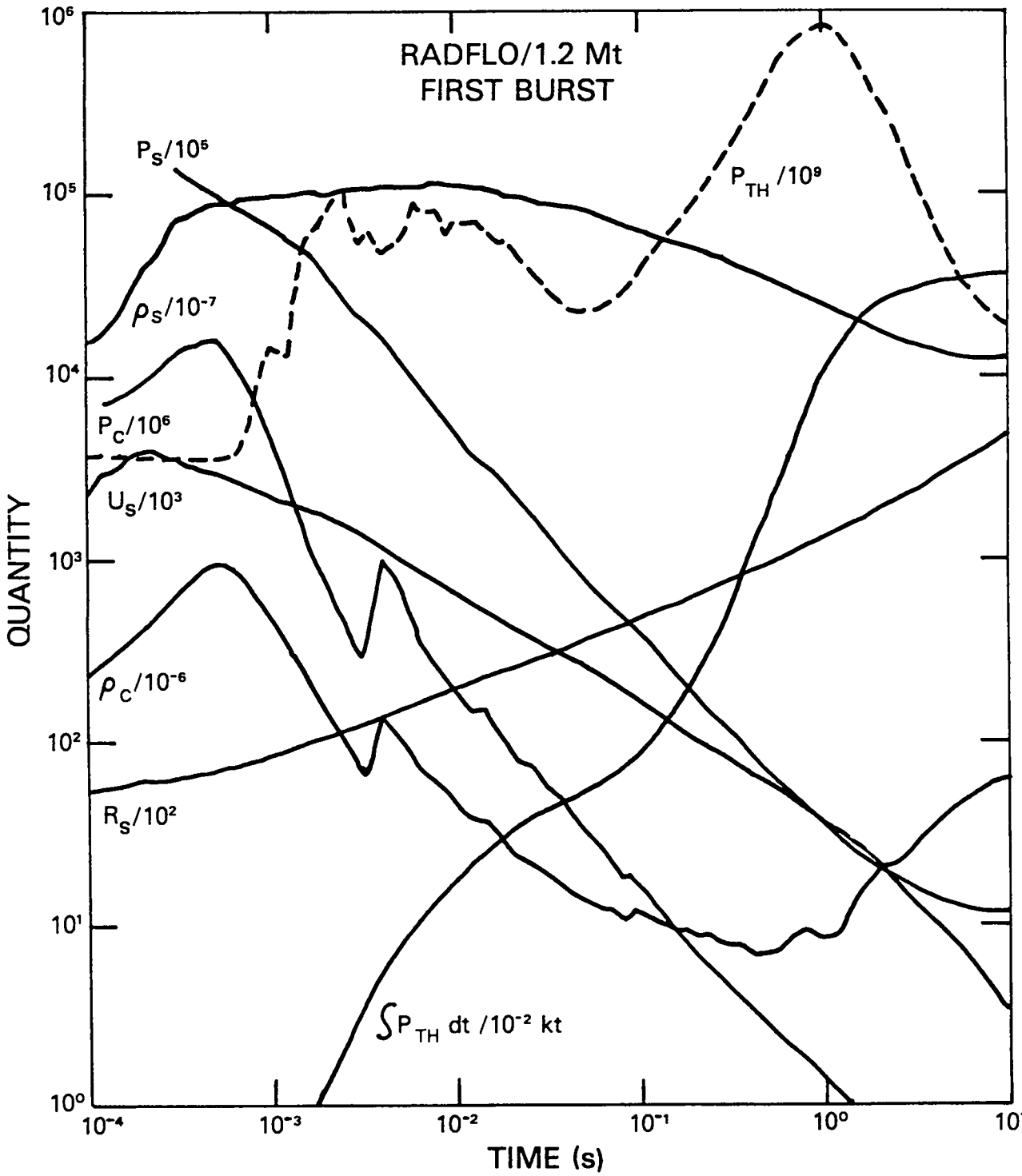

Fig. 2. Summary of the evolution of the first burst. The eight quantities plotted are thermal power (P_{TH}), shock pressure (P_s), shock density (ρ_s), central pressure (P_c), fluid velocity at the shock front (U_s), central density (ρ_c), shock radius (R_s), and integrated power ($\int P_{TH}$). All quantities are given in cgs units. For example, the shock density is 0.01 g/cm^3 near 0.01 s.

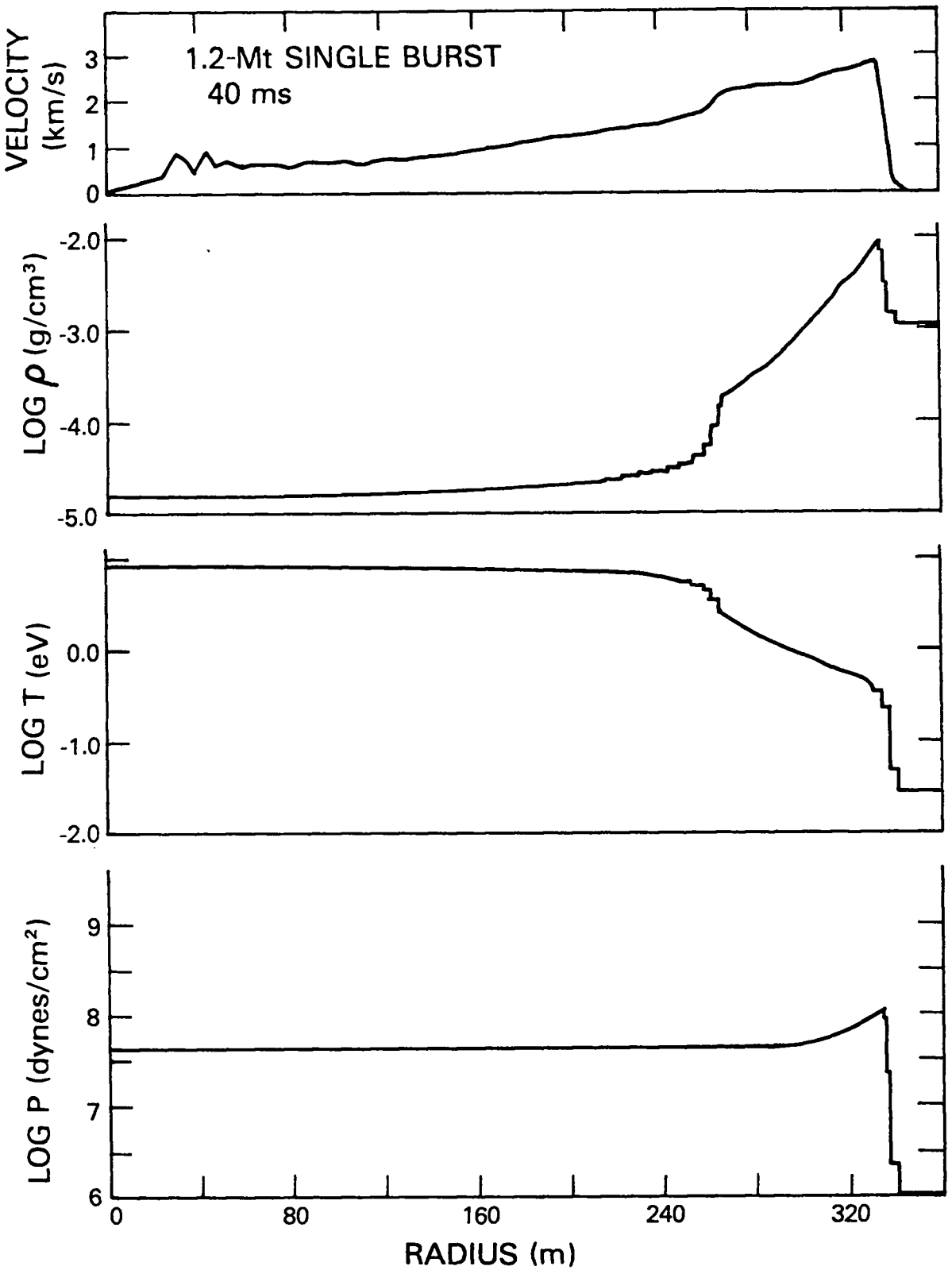

Fig. 3. The flow field of the first burst at 40 ms, at time near minimum when the fireball is well within the blast-wave phase of evolution.

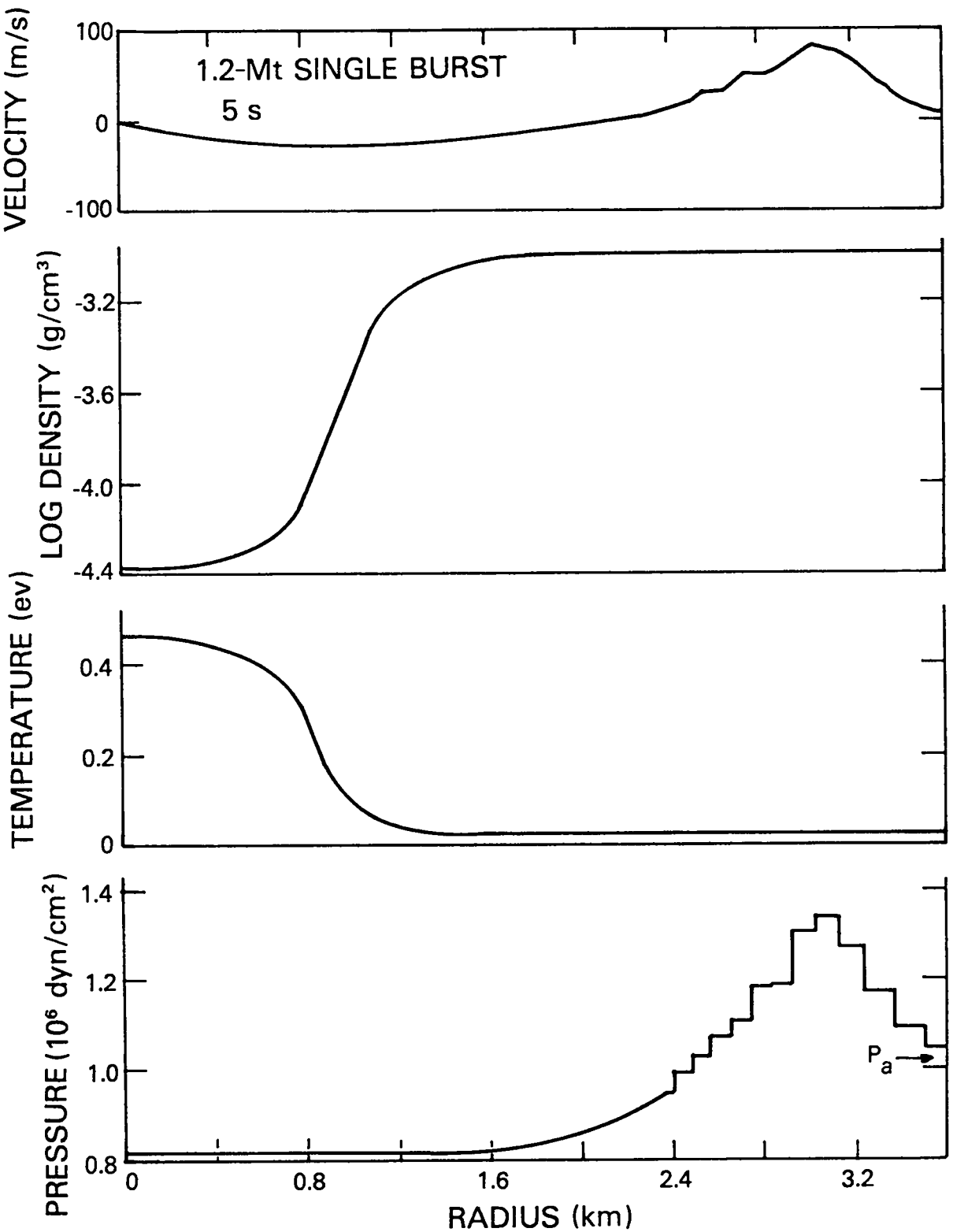

Fig. 4. Flow-field profiles of the first burst at 5 s, just before the second burst. P_a is ambient pressure.

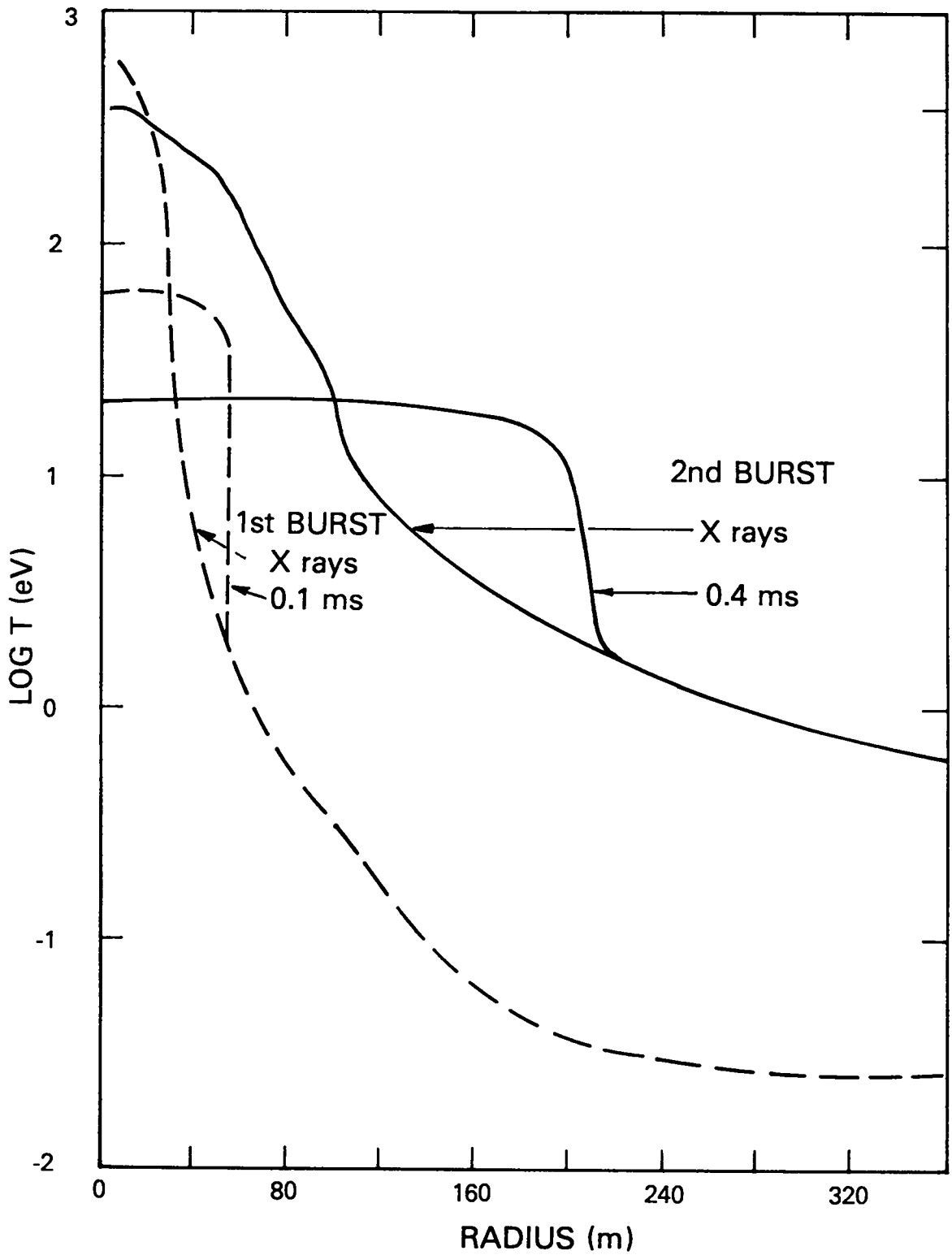

Fig. 5. Radiative growth of the two fireballs. The curves labelled "X rays" show the temperature profiles at the end of the x-ray deposition phase. Radiative expansion continues until the hydrodynamic shocks form at 0.1 and 0.4 ms, respectively. Distances scale with the cube root of density, a factor of 3 between these cases.

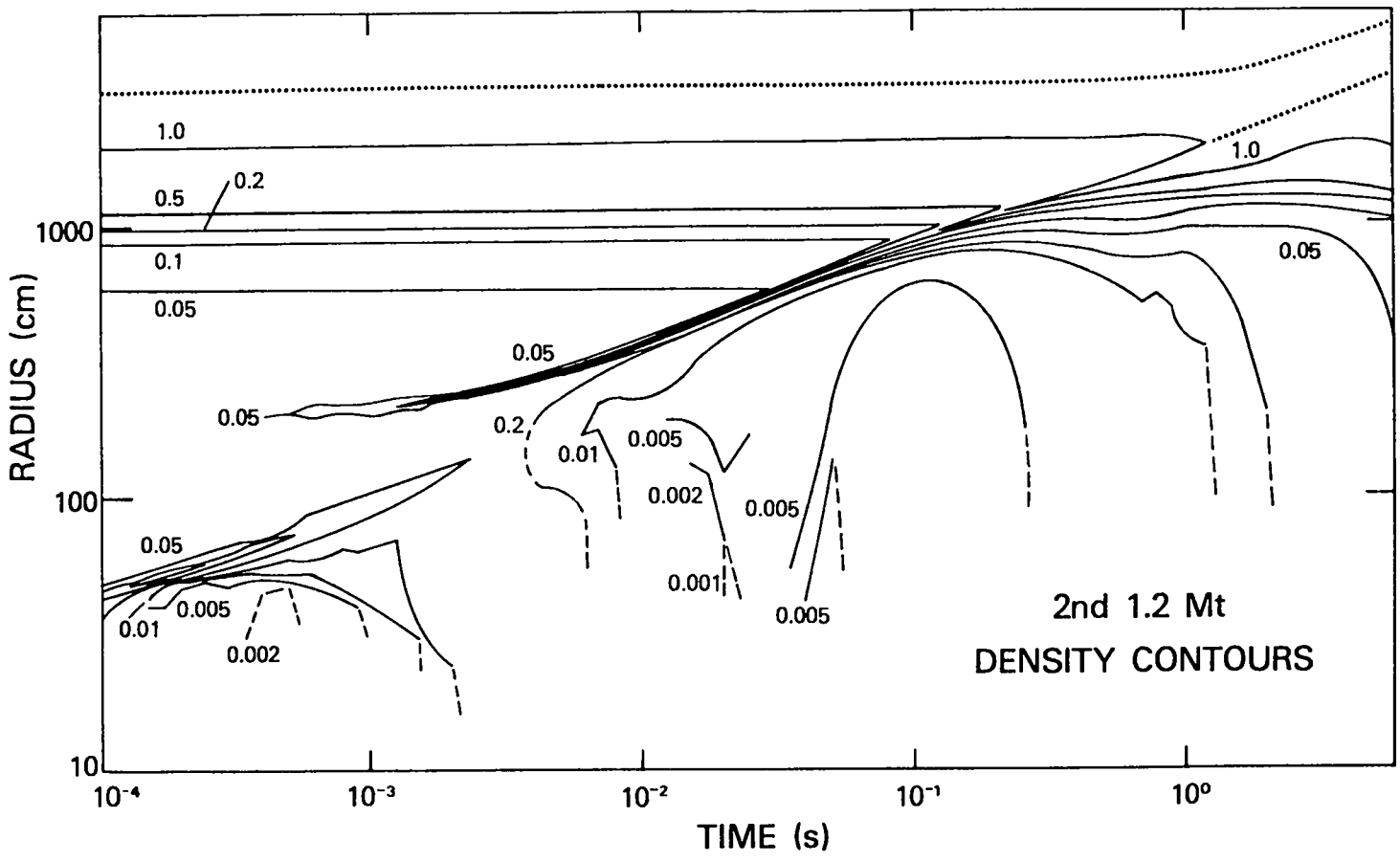

Fig. 6. Density contours following the second burst. Zero time has been shifted 5 s. The signal that dies out near 1 ms and 100 m is the debris shock. The hydrodynamic shock forms about that time at 200 m. The edge of the density well formed by the first burst is evident near 100 m.

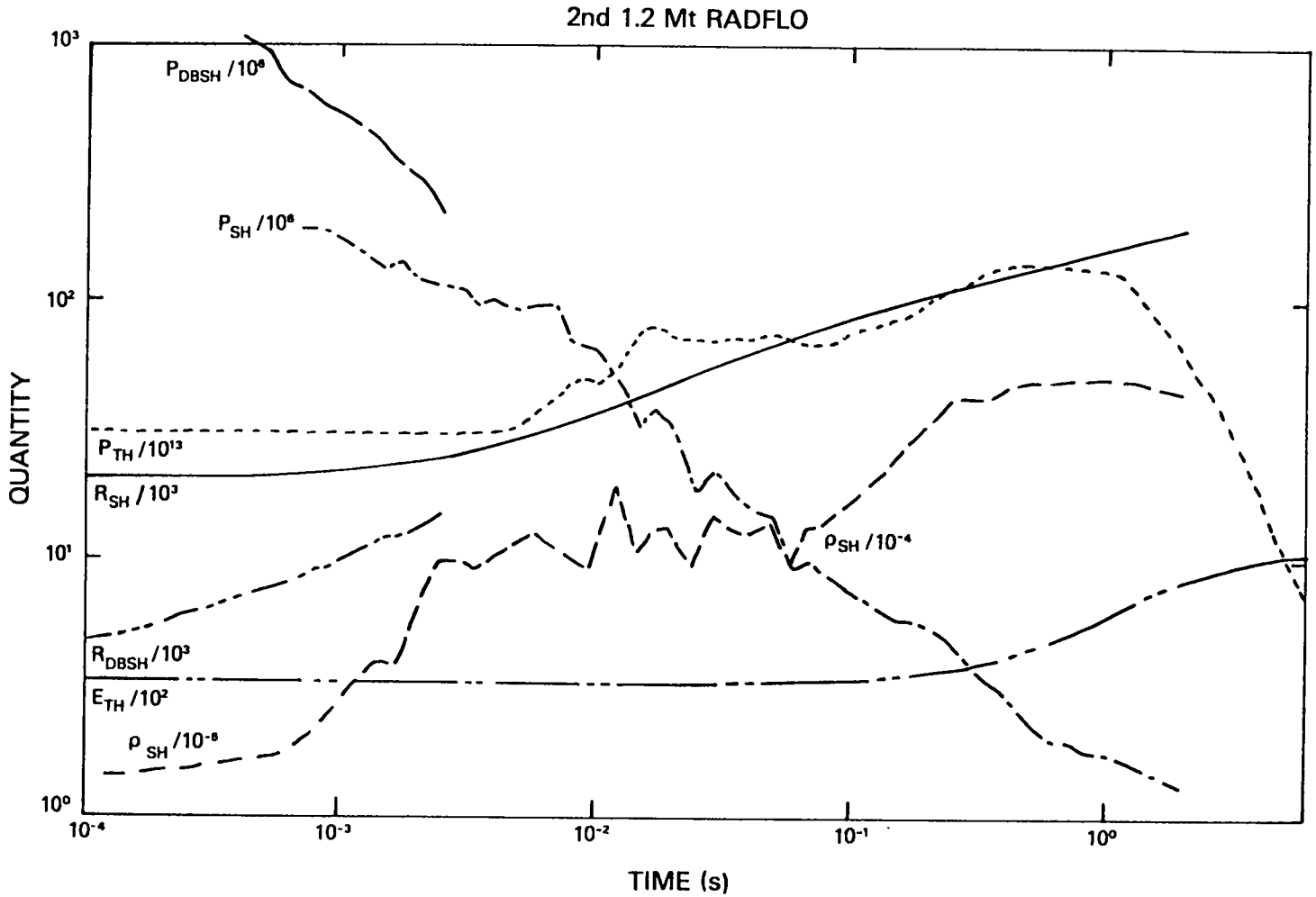

Fig. 7. Summary of the evolution of the second burst. The quantities plotted here are the pressure in the debris shock (P_{DBSH}), main shock pressure (P_{SH}), thermal power (P_{TH}), shock radius (R_{SH}), debris shock radius (R_{DBSH}), integrated thermal power $E_{TH} = \int P_{TH}\, dt$), and shock density ($\rho_{SH}$).

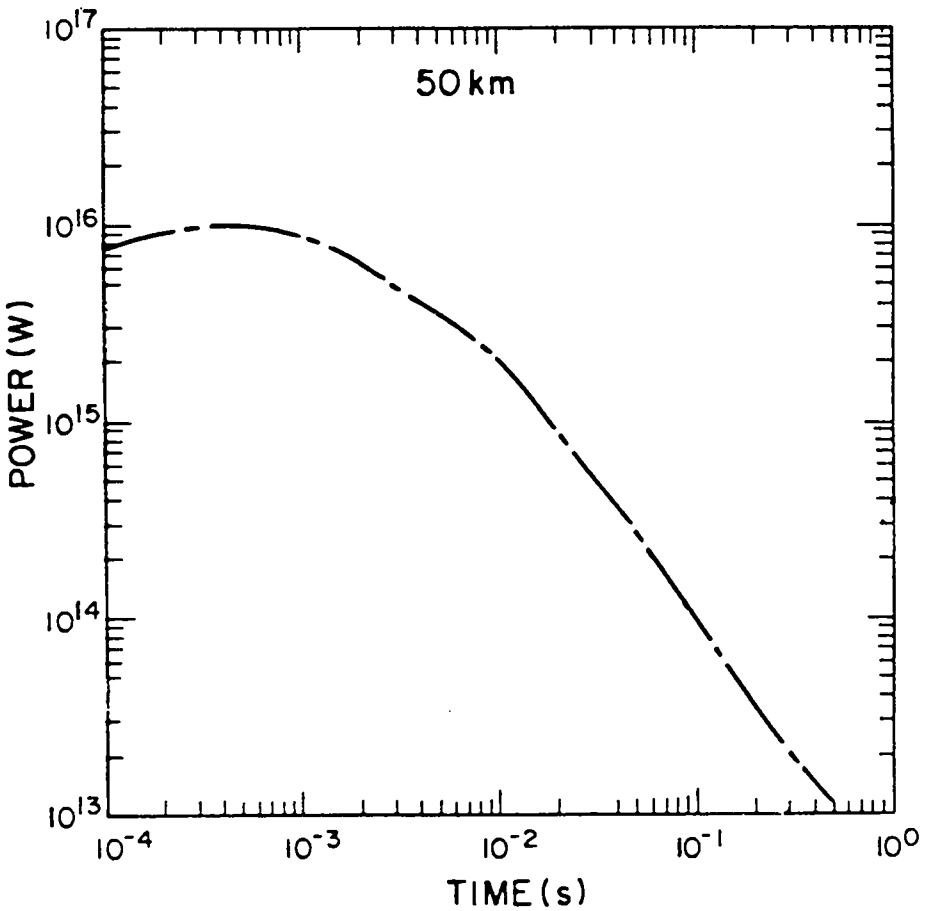

Fig. 8. Power-time history of a medium yield burst at 50 km.

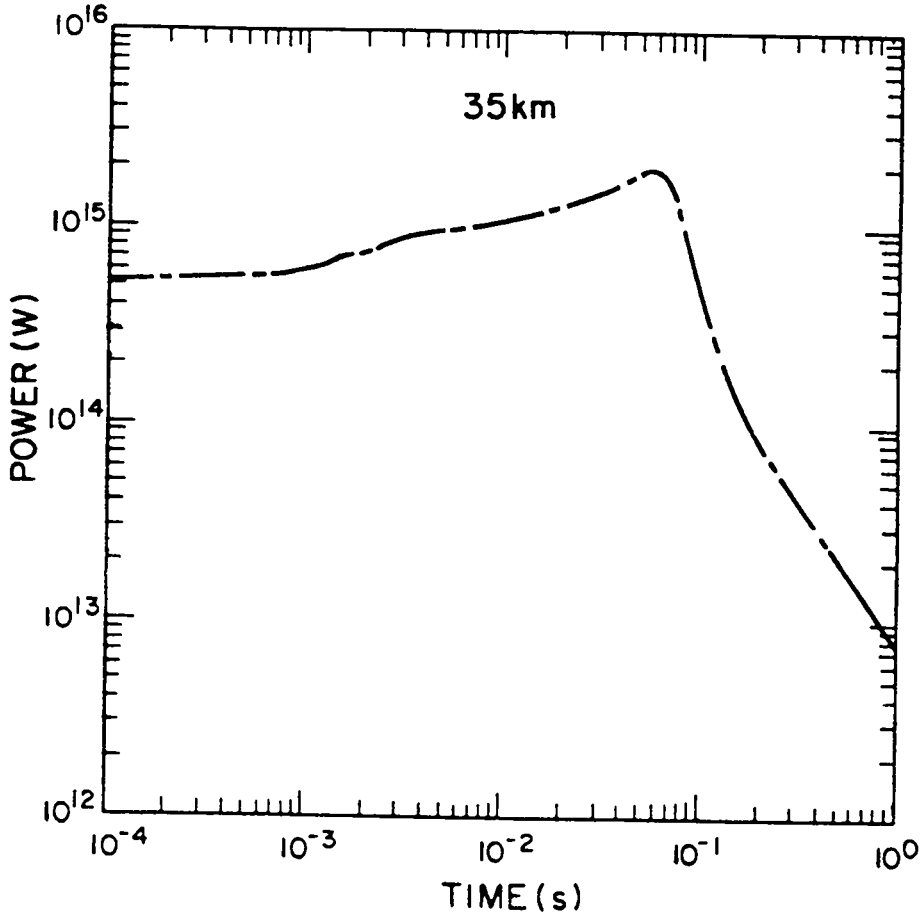

Fig. 9. Power-time history of the same explosion shown in Fig. 8 but calculated at 35 km.

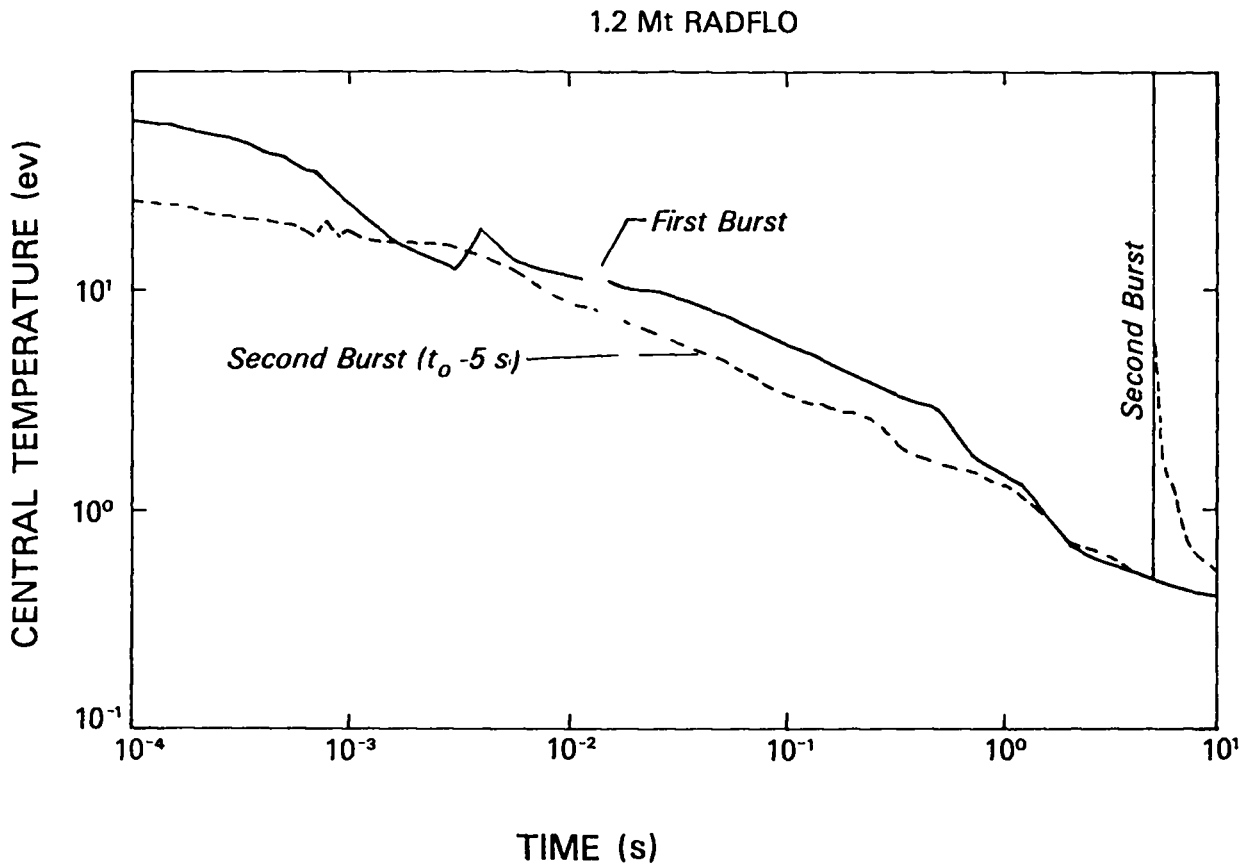

Fig. 10. Central temperature of the two bursts as a function of time. The dashed curve represents the portion of the solid curve after the second burst but with a time shift of 5 s.

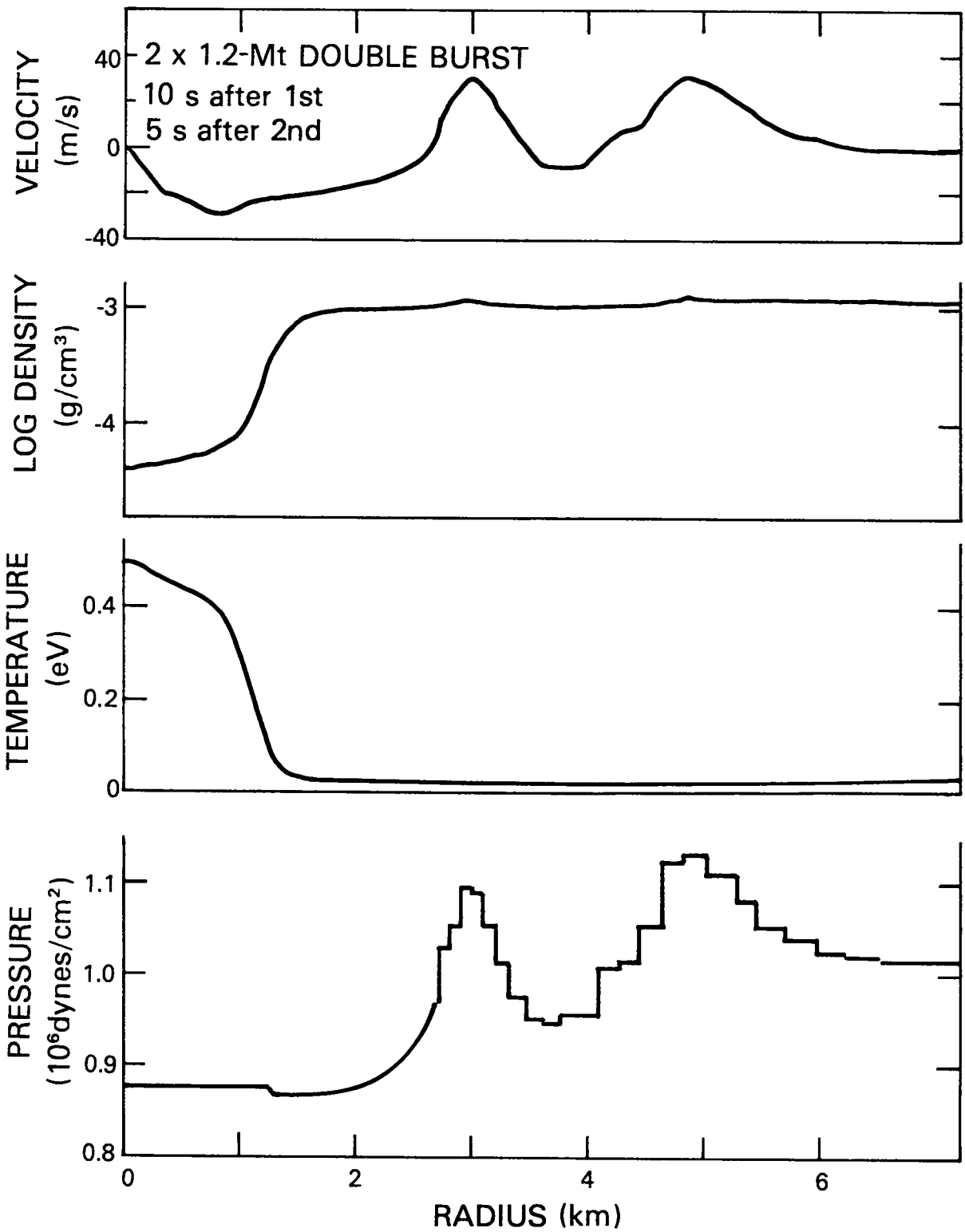

Fig. 11. Flow-field profiles 5 s after the second burst. This figure should be compared with Fig. 4.

Printed in the United States of America
Available from
National Technical Information Service
US Department of Commerce
5285 Port Royal Road
Springfield, VA 22161

Microfiche (A01)

Page Range	NTIS Price Code	Page Range	NTIS Price Code	Page Range	NTIS Price Code	Page Range	NTIS Price Code
001-025	A02	151-175	A08	301-325	A14	451-475	A20
026-050	A03	176-200	A09	326-350	A15	476-500	A21
051-075	A04	201-225	A10	351-375	A16	501-525	A22
076-100	A05	226-250	A11	376-400	A17	526-550	A23
101-125	A06	251-275	A12	401-425	A18	551-575	A24
126-150	A07	276-300	A13	426-450	A19	576-600	A25
						601-up*	A99

*Contact NTIS for a price quote.

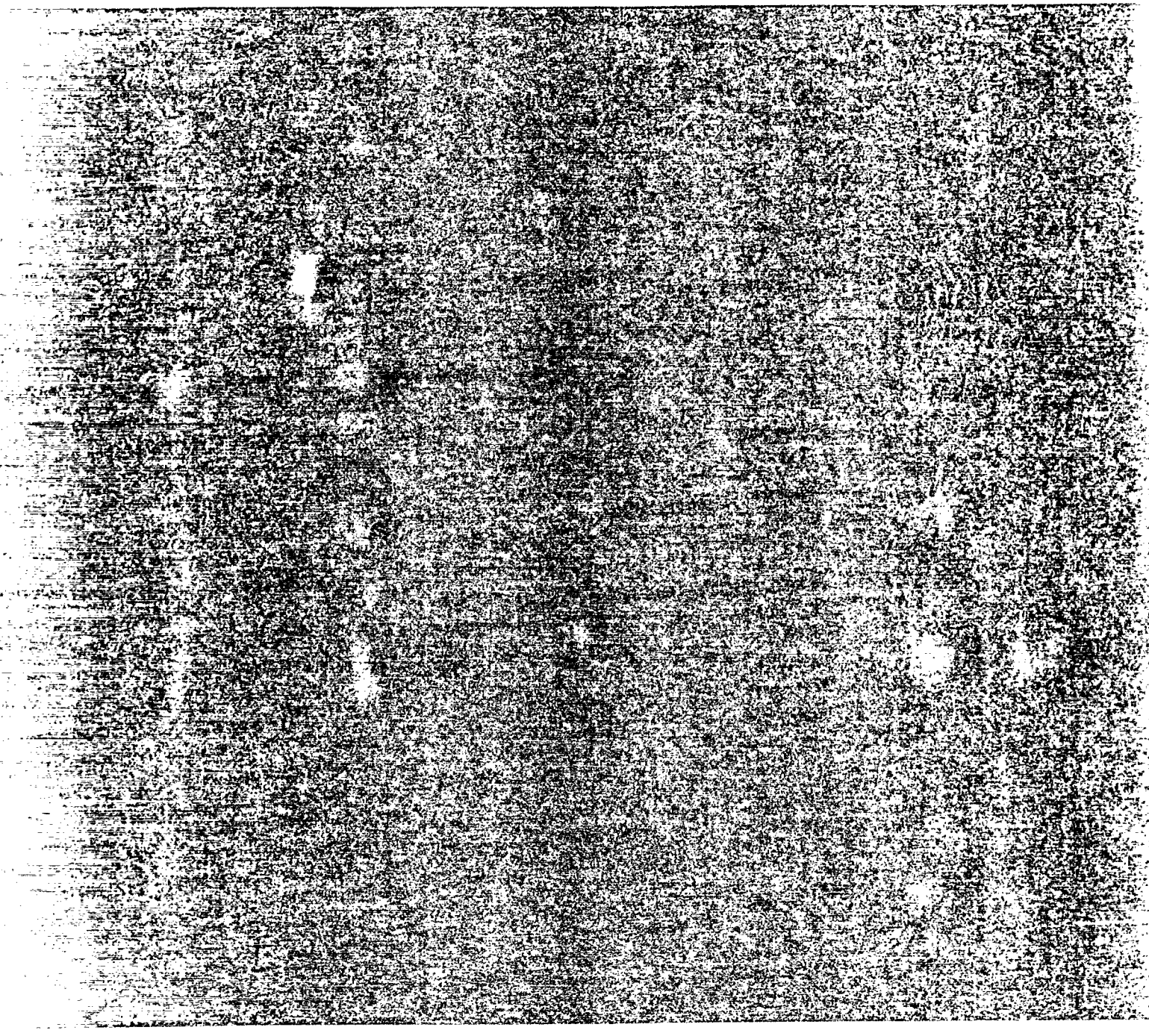

Los Alamos